A multibody dynamics model to assess the impact of road unevenness on the efficiency of a semitrailer truck

Louis Gagnon

Department of Mechanical Engineering,
Laval University,
Québec, QC, Canada
E-mail: louis.gagnon.10@ulaval.ca

Marc J. Richard

Department of Mechanical Engineering,
Laval University,
Québec, QC, Canada
E-mail: marc.richard@gmc.ulaval.ca

Guy Doré

Department of Civil Engineering,
Laval University,
Québec, QC, Canada
E-mail: guy.dore@gci.ulaval.ca

Abstract: An open source multibody model of a semi-trailer truck with 331 degrees of freedom was built and within it a dynamic tyre model has been implemented. The truck model was calibrated and validated by an on road experimental campaign of coastdown tests. There, the signal from a photodetector, 10 accelerometers, the weight distribution, meteorological data, and the longitudinal profile have been collected. The truck model's purpose is to obtain of the relationships between road surface condition and fuel consumption, vehicle wear, passenger health, and security.

Keywords: Multibody Dynamics; Tractor Semitrailer; Experimental Coastdown Tests; Energy Losses; Model Calibration; Road Roughness; Longitudinal Profile; Rigid Ring Tyre Model.

Reference to this paper should be made as follows: Gagnon, L., Richard, M. J., and Doré, G. (2013) 'A multibody dynamics model to assess the impact of road evenness on the efficiency of a semitrailer truck', *International Journal of Vehicle Systems Modelling and Testing*, Vol. x, No. x, pp.xxx–xxx.

Biographical notes: Biographies

1 Introduction

It has been known for a long time that the quality of the road surface has an important influence on the efficiency of the vehicles that operate on it. According to Zaniewski and Butler [30] the cost of repairing a road is 80 times smaller than the increase in vehicle operating costs caused by its poor state. Gagnon *et al*. [9] conclude after conducting a rigorous literature review that the great majority of authors find an decrease in the vehicle efficiency when the road deteriorates. While they mention that the Power spectral density (PSD) may help evaluate the impact of a road profile, they think that a dynamic model would greatly help such analyses.

Without going through the details here, it has been shown that the fuel consumption of a vehicle increases with decreases in surface quality [27, 16, 8, 13, 14, 28, 4, 10, 15, 18]. Impacts on the wear of vehicles [5, 17, 12] and on safety [2, 19, 26, 20, 23] are also shown. Finally, there is also an influence on the health and comfort of the people on board [7, 3]

Han [11] created simple models which calculate the costs associated with the specific waste a road profile will bring about. While his model seems promising and while the Reference Quarter Car Simulation (RQCS) is the most commonly used indicator of a road surface quality through the International Roughness Index (IRI) which calculates the movement a suspension accumulates over a certain profile, both these approaches were not considered accurate enough and a more complex multibody dynamics model was thus created.

The goal of the current project is to develop a multibody model which yields resulting data which allows to assess the specific impact of the road profile on the four criteria of efficiency previously mentioned. The required output data is 1) the torque applied to the driver wheels, for fuel consumption; 2) the forces to which different vehicle components are subjected to and the friction forces at the tyres, for vehicle wear; 3) the vibrations at the driver and passenger seats, for human health and comfort; and, 4) the contact forces between the tyres and the road, for safety.

The developed model will allow vehicle fleet operators to grasp a better idea of the consequences of a specific road on their efficiency. It can also be used by road managers to prioritise specific road sections for repair based on an impact study.

2 Model Description

In order to respond to the need outlined in the introduction, a multibody dynamic model for which a particular attention was given to the dissipation of energy was developed. It allows an accurate representation of a heavy vehicle and the detail of many of its components.

The use of commercial software packages was considered but those cannot give the flexibility the project required. It was also preferred to avoid associated licensing costs to allow anyone to use the model. It was thus chosen to rely on the open-source MBDyn software package which has the basic necessary multibody elements to build a ground vehicle model.

The multibody model has 331 Degrees of Freedom (DoF) and allows to consider individually each component of the 22 wheel tractor semitrailer rig. The mass distribution attempts to reproduce as best as possible the Freightliner Cascadia® tractor and Manac® trailer combination. This combination was chosen because it represents one of the most common heavy truck which circulates on North-American roads and that the manufacturers

have accepted to provide essential technical data. The dampers present between the various components of the vehicle are modelled. Energy losses in the various rotating parts are function of their angular velocity. The tyres are modelled by a rigid ring model that was previously built, calibrated, and validated as a MBDyn c++ module which is accurate in modelling the dynamic response of the tyres to the road profile at frequencies up to 100 Hz.

The tractor has a conventional cabin and the trailer has 3 axles. The following description uses the MBDyn nomenclature. The tridimensional multibody model is shown from the side on Figure 1. Other than the wheels, the vehicle has 13 masses with each 6 DoF: one mass for each axle; one for the tractor chassis frame and the components which are rigidly attached to it such as the batteries and gas tanks; one for the engine; one for the cab; one for the driver; one for the passenger; one for the radiator; one for the trailer frame. The tractor and trailer are linked by a spherical joint free to move in any angular direction. No stiffness is incorporated in that joint because, as noted from the approaches of Falah and Côté [6] and of TruckSim [1], the stiffness is null at low relative roll angles and this is the case for all tested profiles. The radiator is attached to the chassis frame by 2 uncoupled tridimensional translational viscoelastic elements. It is constrained in order to prevent rotation around the lateral axis of the tractor with a cardano rotation joint. The axles are constrained to move only along the vertical axis of the frame and rotate around its longitudinal axis using a inline joint combined with a revolute rotation joint. The engine and cabin are each attached to the frame by 4 uncoupled tridimensional translational viscoelastic elements. The driver is rigidly fixed onto a seat which is attached to the cabin by a unidimensional translational viscoelastic element. It is maintained in the same orientation as the cab by a prismatic joint and is only allowed to move along the vertical direction of the cab by an inline joint. The mass of the driver is distributed between the seat and the floor with proportions of 78% and 22% respectively. Even though Stein *et al*. [25] find that seat cushions do influence the overall stiffness felt by the driver, the cushion was neglected due to a lack of data. It is also assumed that the seat will not be solicited enough to reach the spring stops. Each wheel is attached to its axle by a revolute hinge which only allows rotation around the lateral axis of the axle or intermediate mass. Indeed, the viscoelastic elements of the front wheels are attached to an intermediate mass which follows the wheel orientation but does not roll. It represents the steering system. The effect of the camber angle was found from preliminary tests conducted with TruckSim to be negligible for the intended purpose. Rotation inertia of the brake discs, wheel hub, transmission, and differential are neglected.

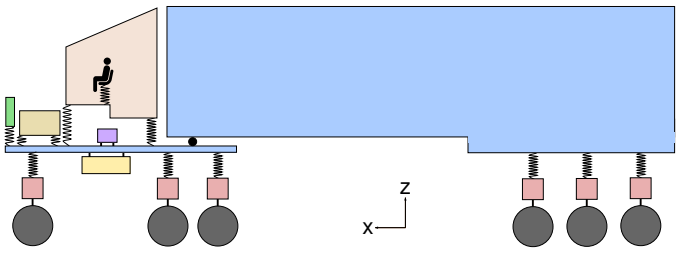

Figure 1 Side view of the tridimensional multibody model.

Figures 2 to 12 present the model assembly just described. Amongst those, Figures 2 to 5 display different zones of the vehicle. Elements L1 to L7 from those figures are expanded in

Figures 6 to 12. Finally, the MBDyn nomenclature and symbols of the figures are clarified in Table 1.

Table 1 Identification of the multibody elements.

Sym.	Element name	Description
C	revolute hinge joint	restrains any relative movement between two rigid bodies except for the rotation about one axis
E	in line joint	forces a point on one body to follow a line attached to a second body
G	centre of mass	in Figures 6 to 12 the centre of mass is connected to the elements when representative of the multibody model
H	cardano rotation joint	forces two bodies to maintain the same relative orientation about one of their axes
P	prismatic joint	forces two bodies to maintain the same relative orientation about all of their axes
R	revolute rotation joint	forces two bodies to maintain the same relative orientation about two of their axes
S	spherical hinge joint	forces points on two bodies to maintain the same relative position
T	total joint	allows to constrain DoF between two bodies based on user defined equations. In Figure 10, all DoF are blocked except for the rotation about the local vertical axis which is governed by a steering function
1	deformable displacement joint (viscoelastic)	applies a unidimensional rectilinear interaction force between two bodies which depends on stiffness and damping coefficients given by the user and the distance between those two bodies expressed in the coordinate system of one the two bodies
3	deformable displacement joint (viscoelastic)	applies a tridimensional rectilinear interaction force between two bodies which depends on stiffness and damping coefficients given by the user and the distance between those two bodies expressed in the coordinate system of one the two bodies
3’	deformable hinge joint (viscoelastic)	applies a tridimensional interaction moment between two bodies which depends on stiffness and damping coefficients given by the user and the relative angles between the two bodies expressed in the coordinate system of one the two bodies

For each run, the truck is started on a completely flat profile. A developed steering control algorithm maintains a straight line trajectory and, when not in neutral gear, a developed cruise control algorithm maintains a constant velocity. No differential is used and the power applied to the drive wheels by the cruise control algorithm is divided evenly. It is important that the trajectory and velocity remain the same over various optimisation trials

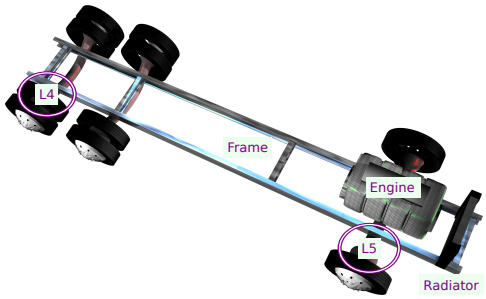

Figure 2 Tractor wheels.

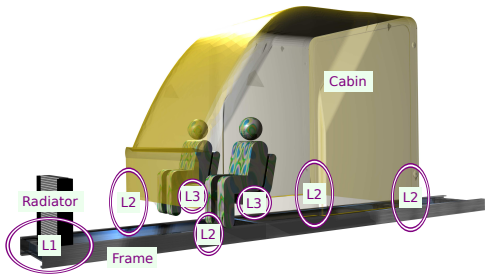

Figure 3 Tractor cab.

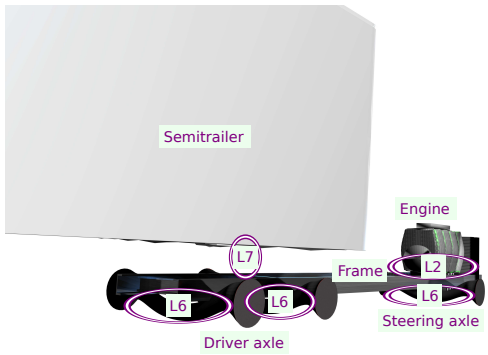

Figure 4 Tractor frame.

because otherwise the results would be influenced by factors other that the parameters of the calibration. That said, once the truck becomes stable after a 5 s period on a completely flat profile, a transition zone allows it to attain the right and left starting elevations of the road profile. At the end of the studied zone, the lateral inclination is brought back to zero and the final elevation is maintained. This procedure is implemented as a modification to the original profile before any filtering is done to it.

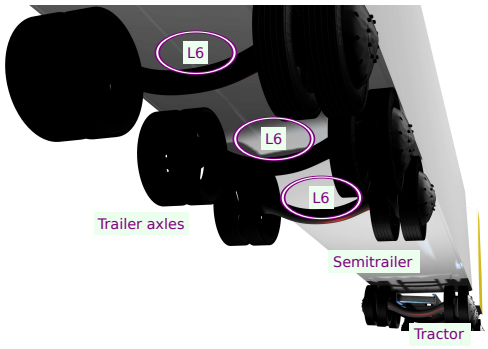

Figure 5 The semitrailer axles.

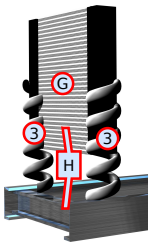

Figure 6 Exploded view of the L1 link between the frame and the radiator.

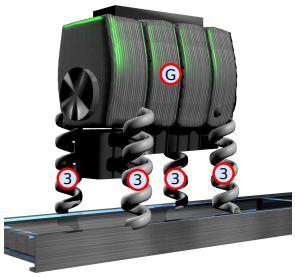

Figure 7 Exploded view of the L2 link between the engine or the cab and the frame.

3 Experimental Campaign

In order to adjust and validate the model, a calibration procedure was deemed necessary. Thus, data was needed and the tractor trailer rig was tested experimentally in real driving conditions. Its behaviour while driving on different road profiles was measured and compared with the numerical model operating on those same profiles. Those experimental runs were done on the *rang Smith* road in Saint-Louis-de-Blandford, Québec. The road has a roughly 3 km straight and flat zone with significant cracks and a strong deterioration level. Yet, the unevenness of *rang Smith* does not surpass levels which are commonly found in

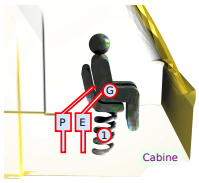

Figure 8 Exploded view of the L3 link between a passenger and the cab.

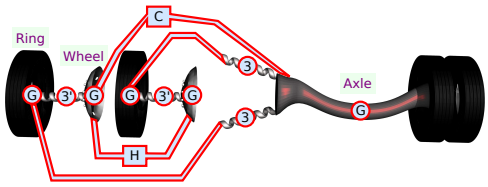

Figure 9 Exploded view of the L4 link between the dual wheels and their axle.

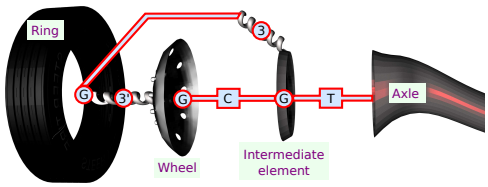

Figure 10 Exploded view of the L5 link between the steering wheels and their axle.

North-America. What also makes that road an ideal place for the tests is that there are no driveways along its side and traffic is minimal. The *rang Smith* is shown in Figure 13.

3.1 Tests description

The actual tests are coastdown tests of a Cascadia® truck with at least 500 km on the odometer to which was attached a curtain walled box semitrailer with 3 axles. The total weight of the duo was 43 t and it was provided by the Centre de formation en Transport de Charlesbourg (CFTC). The legal weight limit for this particular vehicle is 49.5 t. On the *rang Smith*, 2 zones of 518 m and 714 m were selected for the coastdown runs. There, the truck has let itself slow down from an initial speed of 80 km/h in neutral gear. Ten runs were done on each of these 2 zones: 5 in each direction. For these tests, the SAE-J2263 [22] guidelines for coastdown assessments of vehicle load were followed as best as possible and differences from it were deemed reasonable within the context.

The stiffness and damping coefficients, positions, masses, and moments of the various parts were taken from the data given by Freightliner® for their Argosy® truck with a standard semitrailer and they were adapted consequently. Some data was also provided by the CFTC for the details of the specific truck used such as those presented in Table 2. The overall height of the truck was validated by measure at the fifth wheel with consideration for the semitrailer load.

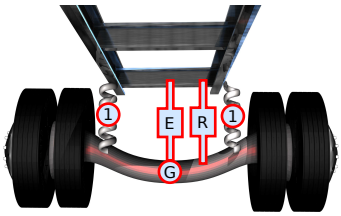

Figure 11 Exploded view of the L6 link between the axles and the tractor or the semitrailer.

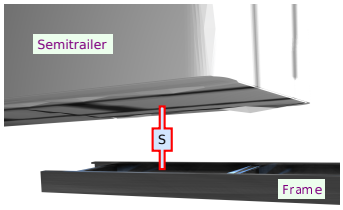

Figure 12 Exploded view of the L7 link between the frame of the tractor and the semitrailer.

Figure 13 Rang Smith in June 2013.

The truck was loaded and instrumented at the CFTC during the days preceding the tests. It was then driven on a 105 km itinerary as a mean of warming up all the components and especially the tyres. The tests on the East road segment were done in the morning and the ones on the West road segment in the afternoon. For the whole day, the winds remained

Table 2 Technical data of the specific truck used for the campaign.

Data	Variable	Value
Engine power	P_{max}	306 kW (410 HP)
Wheelbase	-	533 cm (210 inches)
Differential ratio	D_{fr}	4.11

Figure 14 Lemieux weather station.

calm, it did not rain, and the temperature was 12°C in the morning and 22°C at the end of the day. The winds reached a maximum speed of 13 km/h.

Flagmen located at both ends of the testing zone blocked traffic when the truck was performing a coastdown run. The wheel paths were initially marked by following the truck by foot and spraying white aerosol paint on the road. This allowed the driver to always follow the same path and to read the profile with a Surpro walking profilometer after the coastdown runs were complete. The driver seat stiffness was measured statically at 5716.7 N/m by comparing the elongation of its spring with the driver alone and with added weights. The passenger seat stiffness and camping coefficients were left as given by Freightliner®.

Meteorological data was collected on a 5 m high mast at the Lemieux weather station shown on Figure 14. It is 5 km away from the test site at the same altitude. The immediate surroundings of the station are a brook and fields whereas the surroundings of the *rang Smith* are woods to the North side and a ditch followed by a highway on the South side.

3.2 Collected data

3.2.1 Profile readings

The profile readings were done at the end of the experimental day with a Surpro. Both segments were read with an interval of 1 cm, which covers a portion of the macrotexture. To validate the readings, the same segments were read with a Dynatest van used by Québec's ministry of transportation, the *ministère des Transports* of Québec (MTQ), for the evaluation of their road network. The MTQ readings were done nine months after the Surpro readings.

For the purpose of comparison the Surpro readings were filtered using the same process as the MTQ van profilometer. The profiles match and the small differences are attributed to the frost cycles that occurred during the winter and the small puddles that were present during the van readings. The profile of one track is shown in Figure 15 where the Surpro reading is compared to two readings taken one after the other by the MTQ. The figure makes it visible that the low-pass filter at 91 m which is applied to all readings allows to maintain a null mean vertical displacement and thus cancels out even the small altitude changes on road.

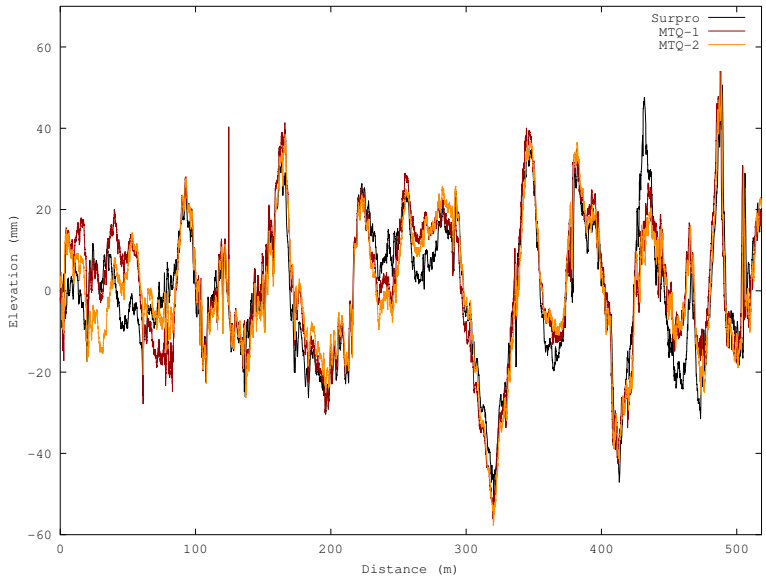

Figure 15 Comparison between the van readings and the Surpro

The lateral elevation differences between the left and right wheel paths were gathered manually and are shown in Table 3. However, due the uncertainty in the lateral drop measured between the left and right track profiles, an approximation was made and the left profiles were each elevated by 5 cm with respect to the right profiles.

Table 3 Lateral elevation differences of the segments at their starts and ends.

Lane	Start (cm)	End (cm)
East	5.25	8.2
West	3.55	4.45

3.2.2 Photodetector

A photodetector is relied upon for the velocity measures because it returns more accurate readings than a radar. Its signal was treated in such a way to obtain the time at which the truck passed in front of the 4 cones that were placed and the start, 10 m after the start, 10 m

before the end, and the end of each road segment. The 4 times are obtained from the peak voltages coming from the photodetector. Table 4 presents the data obtained in this way on the East segment. The variable t_i is the relative time recorded by the sensor at the i^{th} cone, v_i and v_f are the initial and final velocities, respectively. These velocities are calculated using the time taken to travel the 10 m initial and final cone distances. The column E_{kg} is the quantity of kinetic energy per kilogramme of mass of the truck derived from the initial and final velocities. The direction indicated is either going (G) along the traffic or returning (R) against traffic on the segment. The respective initial and final velocity averages when going were 75.5 km/h and 61.7 km/h while when returning they were 77.7 km/h and 58.7 km/h.

Table 4 Data collected by the photodetector during the morning tests on the East segment.

Run	t_1 (s)	t_2 (s)	t_3 (s)	t_4 (s)	v_i (km/h)	v_f (km/h)	E_{kg} (J/kg)	Direction
8	7.11	7.59	44.80	45.41	74.2	59.6	75.4	G
9	9.12	9.59	46.08	46.70	77.24	57.88	100.9	R
10	4.52	4.99	40.80	41.37	76.36	62.61	73.7	G
11	7.85	8.32	45.37	46.00	76.14	57.01	98.3	R
12	4.70	5.17	41.13	41.71	75.97	62.38	72.5	G
13	7.91	8.37	44.65	45.27	77.58	58.37	100.8	R
14	4.37	4.84	40.29	40.86	76.81	63.49	72.1	G
15	5.68	6.14	41.44	42.03	79.16	60.37	101.1	R
16	4.81	5.29	42.26	42.86	73.98	60.61	69.4	G
17	3.42	3.88	39.42	40.02	78.46	60.11	98.1	R

Data from the afternoon tests is shown in Table 5 and the respective initial and final velocity averages when going were 77.6 km/h and 66.0 km/h while when returning they were 77.2 km/h and 66.4 km/h.

Table 5 Data collected by the photodetector during the afternoon tests on the West segment.

Run	t_1 (s)	t_2 (s)	t_3 (s)	t_4 (s)	v_i (km/h)	v_f (km/h)	E_{kg} (J/kg)	Direction
1	5.40	5.87	31.22	31.78	76.53	64.60	65.0	G
2	5.26	5.73	30.77	31.32	77.34	66.26	61.4	R
3	3.21	3.67	28.23	28.77	78.65	67.00	65.5	G
4	6.78	7.24	31.71	32.24	78.76	67.99	61.0	R
5	5.48	5.93	30.18	30.71	79.43	68.09	64.5	G
6	4.18	4.65	29.74	30.29	76.99	66.24	59.4	R
7	6.92	7.40	32.68	33.23	76.45	64.97	62.6	G
8	4.17	4.64	29.92	30.47	76.43	65.72	58.8	R
9	4.47	4.94	30.04	30.59	77.11	65.51	63.8	G
10	6.30	6.77	32.00	32.54	76.52	66.04	57.6	R

3.2.3 Weighting

The truck has been weighted twice without anyone aboard. The first weighting was done with the CFTC scales at the beginning of the campaign day and the second one was done

at the end of the day on the mobile scales of Québec's department of motor vehicles, the *Société d'assurance automobile du Québec* (SAAQ). The SAAQ weightings were rounded at the lowest 50 kg mark. All the weightings are shown in Table 6. One can see that there is 1400 kg more on the right wheels and this equates into a 32 mm lateral offset on the centre of gravity. The weight of the driver was 79 kg, the main passenger 85 kg, and the secondary passenger 70 kg.

Table 6 Experimental weights and tyre data.

Axle group	CFTC (kg)	SAAQ (kg)		Tyres
		L	R	
Steering	5250	2450	2600	XZA-1-LRG
Driving	15720	3800	4050	XDS
		3750	4100	
Trailer	22080	3550	3900	XZE2
		3500	3850	
		3650	3600	

Standard fuel consumption data was used to figure out the burnt mass of fuel was estimated at 62.2 kg for the morning runs and at 99.9 kg for the afternoon runs. The last weighting of the day was done after driving 77 km away from the test segments and the lost mass of fuel reached 146.2 kg.

The XZA3 is the tyre that was was calibrated within the tyre model. Weights of different tyres from Michelin® are shown in Table 7 where versions of tyres XZA-1, XDS and XZE2 were chosen as being 27.9 cm (11 inch) wide and having a 57.2 cm (22.5 inch) radius. The data shown is for the 14 ply version of the XZE2 tyre.

Table 7 Factory weight of the various tyres used during the tests.

	XZA-3	XZA-1	XDS	XZE2
Weight (kg)	51.5	53.3	60.7	53.9
Radius under load (mm)	47.50	49.02	49.53	49.02
Radius (mm)	50.93	52.54	53.09	52.54

3.2.4 Sensors

The accelerometers and their various natural frequencies are shown in Table 8. Columns f_{minE}, f_{maxE}, and f_{mE} are the minimum, maximum, and average first natural frequencies recorded experimentally on each segment. The column Axis gives the direction in which each accelerometer records vibrations. The suffix C indicates that the 65 m were removed from the response in order to ignore the lagging effects of the road surface located before the segment of interest. The Seat accelerometer was located behind the seat on the rigid support which holds the cushion. The Rear Axle accelerometer was installed under the rear driving axle to the left of the truck and is shown in Figure 17. The Floor sensor was installed on the cabin floor on the right edge of the gear stick. The Rear Triaxial sensor was installed on the chassis frame crossmember located between the steering and driving axles. The Front Triaxial sensor was installed at the centre of the steering axle and the

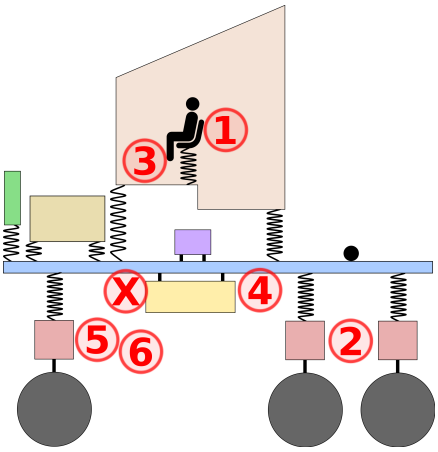

Figure 16 Sensor layout where x is for the photodetector.

Figure 17 Rear Axle sensor.

Front Axle sensor was installed on its right edge. The two sensors on the steering axle are shown in Figure 18. Finally, the photodetector was installed on the left tractor step, as shown in Figure 19. Figure 16 gives the approximate disposition of each sensor and obeys the numbers of Table 8.

The accelerometers used in the experimental campaign produce a 5% error due to the vibrations along the axes perpendicular to the one considered. This error remains small for the acceleremoters presented here because the signal amplitudes in the three axes were similar, as can be seen by comparing the magnitudes on Figures 22 and 23.

3.2.5 Wind

The East segment when going and the West segment when returning both point 48° east of north whereas the West segment when going and the East segment when returning point 132° west of north. Table 9 presents the wind data for different runs and gives the origin of the wind as the angle from the north in clockwise direction. Based on the winds recorded during the campaign, the calculated maximum possible wind induced influence on the total energy consumption of the tractor is 1.2 J/kg. The effect of wind resistance could however be quite important. For example a 1.6 fold increase of the drag coefficient which would be

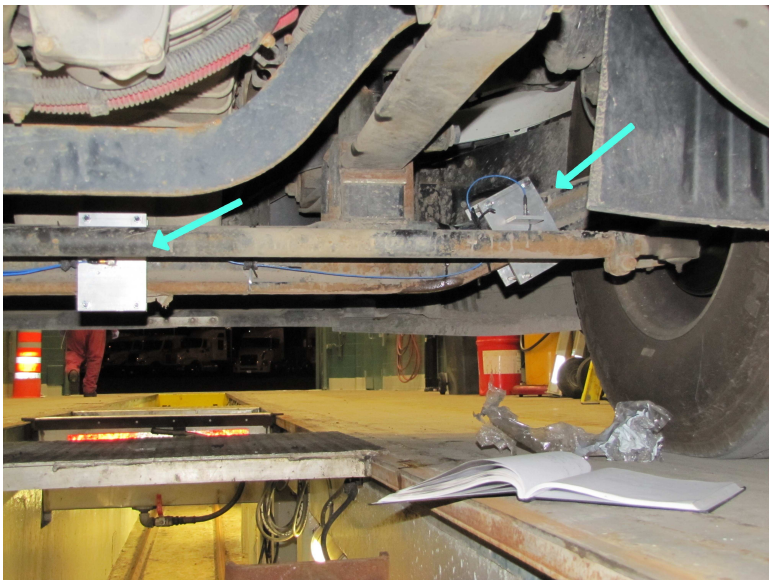

Figure 18 Sensors of the front axle.

Figure 19 Photodetector.

Table 8 Minimum, maximum, and average first natural frequencies of sensors.

Sensor	N°	Axe	f_{minE}	f_{minEC}	f_{maxE}	f_{maxEC}	f_{mE}	f_{mEC}
Seat	1	z	1.64	1.54	2.15	2.12	1.84	1.86
Rear Axle	2	-z	9.13	9.55	14.31	12.11	10.39	10.81
Floor	3	z						
Rear Triaxial	4	-y						
Front Triaxial	5	-y	11.06	11.57	12.82	12.89	11.98	12.81
Front Triaxial	5	-x						
Front Axle	6	z	10.03	9.99	12.23	11.99	10.83	11.37
Rear Triaxial	4	-z						
Rear Triaxial	4	-x						
Front Triaxial	5	z	9.74	9.57	13.35	13.09	11.38	11.78

caused by a side wind can induce a roughly 4 km/h additional velocity loss over a 700 m segment.

Table 9 Direction and speeds of wind by segment.

Segment	Period	Speed (km/h)	Origin (°)
East return	11h15-12h15	9	190
East going	11h15-12h15	9	190
West going	3h07-3h50	11-13	140-180
West return	3h07-3h50	11-13	140-180

4 Calibration and Validation

The parameters necessary for the multibody analysis of an Argosy® truck as given by Freightliner® were adjusted for the Cascadia® tractor and Manac® semitrailer combination. This data allowed starting the calibration procedure with good approximate data before optimising. The target velocity at the first cone crossing was 21.4 m/s.

The definition for the coefficient of determination, R^2, used to determine the accuracy of the response is,

$$R^2 = 1 - \frac{\sum\limits_i (\zeta_i - \eta_i)^2}{\sum\limits_i (\zeta_i - \overline{\zeta})^2} \tag{1}$$

where ζ and η are the reference curve and the curve to be fitted, respectively. The value $\overline{\zeta}$ is the average of ζ.

4.1 Signal processing

The optimisation was done while considering the acceleration responses against position, the lost kinetic energy along the section, and the natural frequencies recorded by the sensors. The mass subjected to the linear kinetic energy is the mass of the full truck.

The acceleration signals of the first run on each section were converted from being against time to being against position with the help of a cubic polynomial having the form $x_{\text{photo}} = \sum\limits_{n=0}^{3} a_{\text{ph}}^n t_{\text{photo}}^n$ where x_{photo} is the photodetector position, $a_{\text{ph},n}$ are the polynomial coefficients to optimise, and t_{photo} is the time. It estimated the position along the section from the 4 times recorded by the photodetector. That function was also used as a starting point in an optimisation of a 9$^{\text{th}}$ order position function polynomial having the form $x_{\text{photo}} = \sum\limits_{n=0}^{9q} a_{\text{ph}}^n t_{\text{photo}}^n$. It ensured that the peaks in the remaining Front Axle signals, filtered in time by a 2$^{\text{nd}}$ order bandpass Butterworth filter between 14 Hz and 20 Hz, in position matched the first one. Once 5 signals against position were obtained for each accelerometer, the average for each accelerometer and each section was taken as the definitive acceleration against position signal. Then, the 40 signals thus obtained were treated by a 2$^{\text{nd}}$ order low-pass Butterworth filter having a cutoff frequency of 2 m^{-1}, which corresponds to roughly 32 Hz, before being used to optimise the numerical response.

4.2 Weight distribution

The available weight distribution data of the Argosy® tractor was first modified to represent a Cascadia®. Helped by some assumptions and the available data, the mass of the Argosy® frame was calculated at 1204 kg. The Cascadia® wheelbase is 83.8 cm longer and its nose is estimated to be 25 cm longer. Extrapolation of this data yields a 1393.5 kg tractor frame weight. The masses and moments of the other truck components were adjusted in a similar fashion.

The static deflections were calculated according to the weight on each spring. It is assumed that variable static deflections physically represent the distibution of air in the suspension cushions. For example, the front cabin springs' deflection δ is,

$$\delta = \frac{m_{\text{cab}} d_{\text{cab}} \text{g}}{2k_{\text{z,cabF}}} \tag{2}$$

with

$$d_{\text{cab}} = \frac{x_{\text{cab}} - x_{\text{cabR}}}{x_{\text{cabF}} - x_{\text{cabR}}} \tag{3}$$

where $k_{\text{z,cabF}}$ is the stiffness of the front cabin springs, g is the gravitational constant, m_{cab} is the cabin mass including the passengers. The variables x_{cabF}, x_{cab}, and x_{cabR} are the longitudinal positions of the springs that support the front of tha cabin, its center of mass, and the springs which support its rear, respectively. This relation is derived from a static free body diagram of the cabin.

The weight under each wheel was then optimised using the SAAQ measures. An algorithm varied the position of the center of mass of the trailer and the static deflection of every suspension while respecting the total weight on each axle group as obtained at the CFTC. These loads were then adjusted for the fuel losses incurred during the day. The optimisation was done by evaluating the normal forces under each wheel of the truck travelling at steady state on a flat road at the target velocity of the experimental runs. The objective function f is thus the following,

$$f = \sum_{i=1}^{12} |W_{s,i} - W_{e,i}| \tag{4}$$

where i represents the wheel for which the difference in weight is measured. Ten of those wheels are dual. The variables W_s and W_e represent the weights calculated by the simulation and those obtained from the SAAQ data, respectively. The weight distribution obtained by this procedure gives an accumulated absolute error of less than 200 kg over the 12 wheels.

4.3 Coefficients to optimise and objective function

A series of objectives were tested before choosing a definite one. Amongst those was one that neglected raw acceleration versus position signals and compared the fast Fourier transforms obtain from the experimental and model signals. Another approach was to calibrate based on the amplitude of the natural frequency but this approach had issues with the somewhat random distribution of frequencies around the natural one which tends to have a strong

influence on its amplitude, as can be seen when comparing the experimental Figure 22 to the model Figure 21 (d) which both display the same sensor signal.

The contribution of kinetic energy Φ to the objective function is given by the following equation,

$$\Phi = \frac{\sum_{i=1}^{4} (\Delta E_{ki})^2}{25} \tag{5}$$

where ΔE_{ki} is the difference in kinetic energy lost per kilogramme of mass between the simulation and the average of the runs on section i. The summation is done on the 4 sections tested.

The values used for the weighting of the time, W_{t}, and frequency, W_{f}, sensor signals are shown in Table 10.

Table 10 Weighting applied to the various signals.

Sensor	Axis	W_{t}	W_{f}
Seat	vertical	1	3
Rear Axle	vertical	1.5	2
Floor	vertical	0.75	0
Rear Triaxial	lateral	0.25	0
Front Triaxial	lateral	0.25	0.5
Front Triaxial	longitudinal	1.25	0
Front Axle	vertical	1.5	2
Rear Triaxial	vertical	1.5	0
Rear Triaxial	longitudinal	1.25	0
Front Triaxial	vertical	1.5	2

These weighting factors come from a careful examination of the importance of each signal, the quality of the experimental data, and the interdependence of the various signals. For example, it was chosen to privilege position signals for the longitudinal response because the frequency signals were deemed less accurate due to the use of dynamic accelerometers. Contrarily, the seat signal was considered more important in frequency because this is how the health impact is measured. Also, the vertical responses at the front and rear axles, the frame, and the floor were deemed important because they all influence the response of the seat. Furthermore, while maintaining it small enough not to completely drown the other parts of the objective function, the importance given to the kinetic energy is relatively high because properly calculating fuel economy impacts due to road roughness was crucial to the project. Thus, the weightings are applied to each sensor for each of the 4 calibration sections and are then summed,

$$P = \sum_{i=1}^{4} \left(\sum_{j=1}^{10} \left(W_{\mathrm{f},j} \left(\frac{|f_{\mathrm{mS},ij} - f_{\mathrm{mEC},j}|}{f_{\mathrm{mEC},j}} + f_{\mathrm{b},ij} \right) \right) \right) \tag{6}$$

where f_{mS} is the natural frequency of the simulation and f_{mEC} is the average experimental natural frequency excluding the first 65 m, as given in Table 8. The index j is the sensor

being studied and f_{b} is a Boolean expression which is null when f_{mS} is located between f_{minEC} and f_{maxEC} and otherwise has a unit value. The contribution of the position signals is,

$$S = \sum_{i=1}^{4} \left(\sum_{j=1}^{10} \left(W_{\mathrm{t},j} \left(1 - R_{ij}^2 \right) \right) \right) \tag{7}$$

where R^2 is the coefficient of determination between the position signals of the simulation and of the averaged experimental data. The final objective function O is thus,

$$O = (\Phi + P + S) \tag{8}$$

and a strong penalty is applied by setting $O = 1 \times 10^6$ when the multibody calculation does not converge. Finally, the specific parameters which have been optimised are the adjusting factors for the drag coefficient, parasitic wheel hub losses, neutral gear transmission losses, and differential losses. The stiffness and damping coefficients of the steering axle suspension, drive axles suspension, trailer axles suspension, front and rear cabin supports, and driver seat suspension have also been optimised.

4.4 Results and Discussion

A selection of experimental data is compared to the results obtained from the calibrated model. The fast Fourier transform of the model acceleration response at the seat is shown on Figure 20 where the vertical bars show the minimum and maximum natural frequencies measured experimentally. Similarly, the simulation frequency responses at the position of the Rear Axle, Front Triaxial and the Front Axle accelerometers are shown on Figure 21 (a), (b), (c), and (d). The presented results are selected amongst the 4 segments because they barely differ between segments and the repeatability of the runs was good. Figures 22 and 23 give a more deeper insight in the frequency contents of both simulation and experimental data.

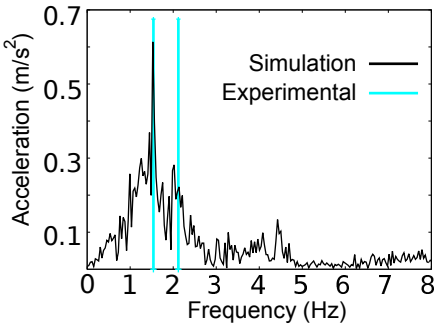

Figure 20 Vertical seat acceleration of the simulation on the West return segment where the vertical bands delimit the minimum and maximum experimentally recorded natural frequencies: 1.54 Hz and 2.12 Hz.

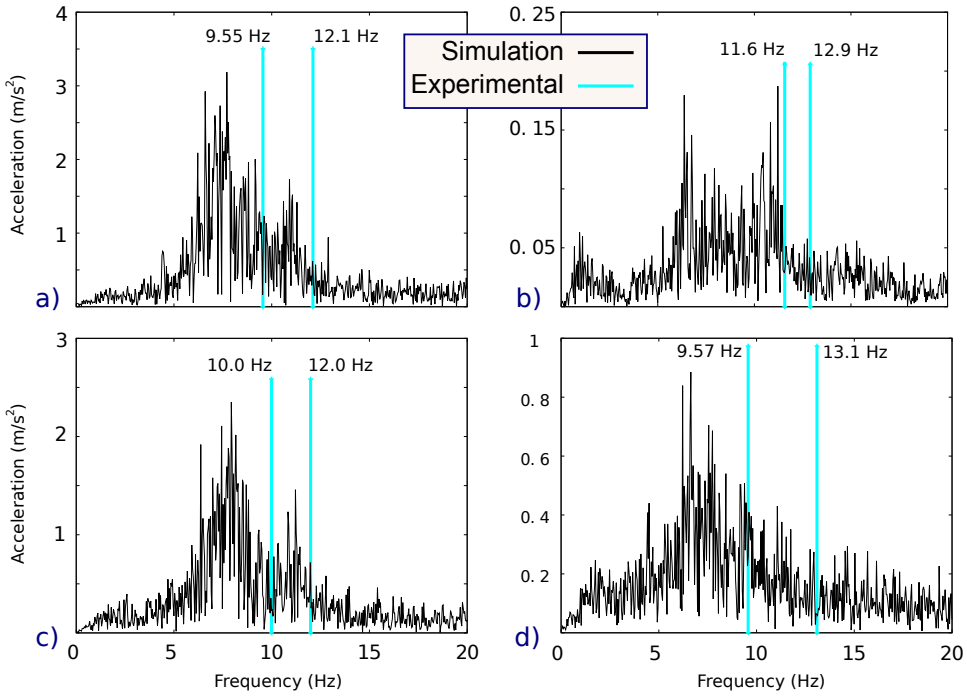

Figure 21 Simulated accelerations on the West segment. a) Vertical on the left edge of the rear axle when returning, b) lateral at the centre of the front axle when going, c) vertical at the right edge of the front axle when going and, d) vertical at the centre of the front axle when returning.

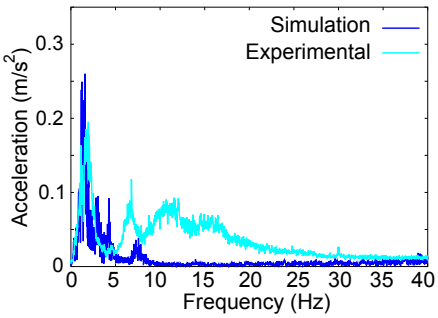

Figure 22 Vertical response of the Front triaxial sensor on the Est going segment.

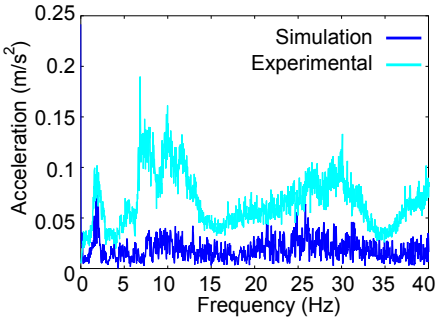

Figure 23 Longitudinal response of the Front triaxial sensor on the West return segment.

Longitudinal responses obtained from the triaxial accelerometers are not reproduced as well as the vertical ones. Yet, the dominant horizontal frequencies correlate quite well, as seen on Figure 23. The difficulty rather comes in reproducing the proper frequency signal amplitude. Moreover, the figure also shows a null frequency contribution for the simulation which does not appear in the experimental data. This null frequency response represents the constant loss of velocity induced by the coastdown procedure. The dynamic accelerometers used experimentally cannot capture such low frequencies. For that reason, their signal was not used to calibrate or validate the energy losses. Figures 20 and 22 outline the strong ability of the model to reproduce the vertical experimental natural frequencies. Figures 21 (a), (c), and (d) also show a good concordance between model and experimental in the vertical axis.

Also, the responses of observed frequencies in simulation and experimental often show crest matches. This phenomenon is particularly visible when one of the responses exhibits its first natural frequency at the observed point. Further testing revealed that the natural frequency observed on a segment 1) varies along the trajectory; 2) is less clearly defined; and, 3) differs from the one on a smooth road. Nevertheless, the natural frequencies measured on the segments of the experimental campaign while including the whole segment or while cutting the first 65 m are very similar.

According to the results of the multibody simulation, the frequencies observed at the axles do no reach beyond 160 Hz and those at the seat beyond 60 Hz. Experimentally, some contributions were detected at up to 600 Hz for both the axles and the seat. Such high frequencies are associated with the flexible vibration modes of the truck's structure. Given that and for simplicity, only the first natural frequencies are considered in the calibration process.

Being raw results which further confirm the excellent correspondence between experimental and simulation, the response versus position plots are shown for a selection of sensors on Figures 24 to 28.

The frequencies given in Hertz on those figures are approximations because the truck velocity actually reduces throughout the coastdown run. First of all, the seat response is plotted on Figure 24 where a filter is applied to focus on the part of the signal which dominates health impacts. When filtered at high frequencies or unfiltered, the experimental signal exhibits noise which may be partly attributed to the vibrating components of the tractor and flexible vibration modes. However, the noise does not take more importance than the low frequency signal as can be noticed on Figure 25 which shows the Front Axle sensor's response. That noise is also found to have a frequency above 60 Hz, which indicates

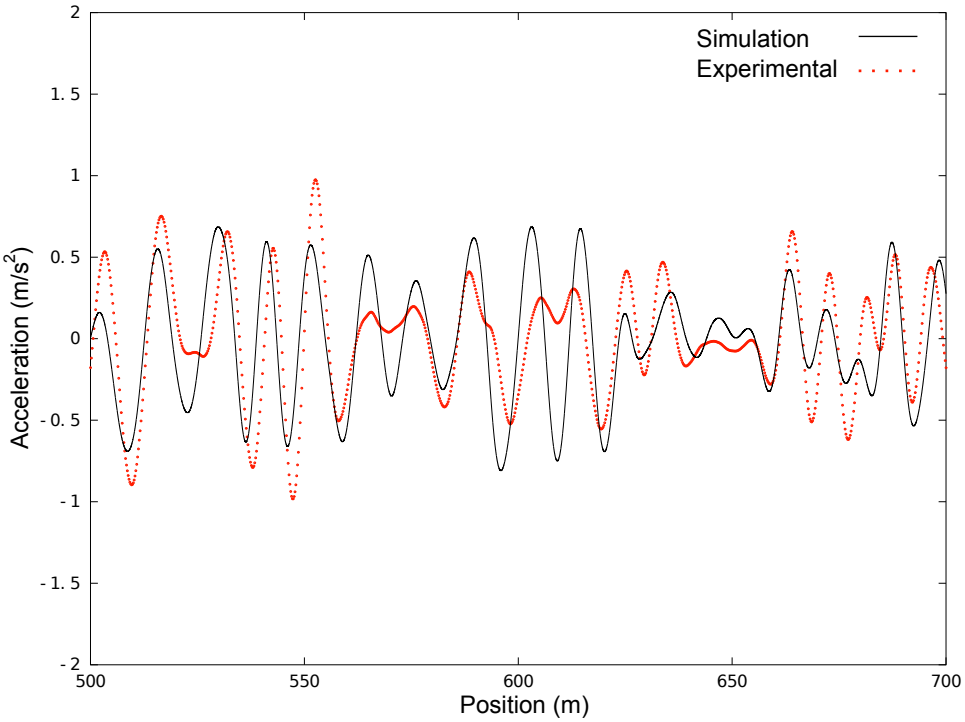

Figure 24 Seat sensor response on the East going segment. Filtered to keep frequencies below one-tenth of an oscillation per meter of road, which roughly corresponds to 2 Hz.

that it can be ignored in this road vehicle impact study. Its effects on health will be negligible and it is likely not cause by road deformations because Sayers and Karamihas [24] pointed out that road deformations of less than 25 cm in length are absorbed by the tyre. Figure 25 also emphasises how the model excels at reproducing the dynamic vehicle response to road unevenness by a very similar behaviour numerically and experimentally. Having two accelerometers on the front axle confirmed the validity of the vertical experimental data.

Although the model diligently reproduces the Front Triaxial accelerometer's natural frequency in the lateral direction, it does strongly underestimates the amplitude of the signal. Surprisingly, the amplitude of the lateral signal at the Rear Triaxial accelerometer is well modelled, as shown on Figure 28. A possible explanation for this phenomenon is that the Rear Axle signal's is taken on the chassis frame while the Front Triaxial signal is taken at the axle. This could thus imply that the lateral vibrations at the frame are dampened by the suspension in the experimental data while they would be dampened at the tyre in the simulation. The vertical responses at the Floor and Rear Axle sensors are reproduced quite well, as presented on Figures 26 and 27, respectively.

Finally, when taking into account that the differences between simulation and experimental in the frequencies obtained for vehicle simulations by Xu *et al.* [21] reach 28% and that the ones of Wasfy *et al.* [29] reach 20%, the results shown on figures 20 to 23 seem very good. For example, the error on the natural frequency between simulation and experimental is roughly 30% for the Seat and Front Axle sensors. This error margin is especially reasonable given the complexity of the model which 1) is calibrated using

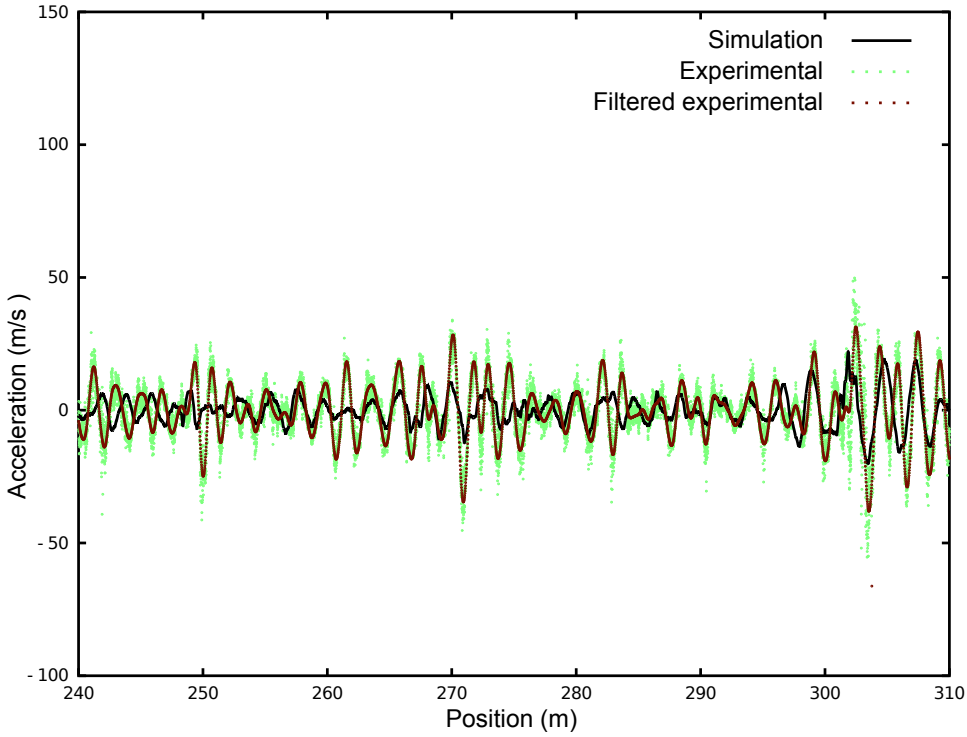

Figure 25 Front Axle sensor response on the West return segment. The filtered experimental response preserves only frequencies below one oscillation per meter of road, which corresponds to roughly 20 Hz.

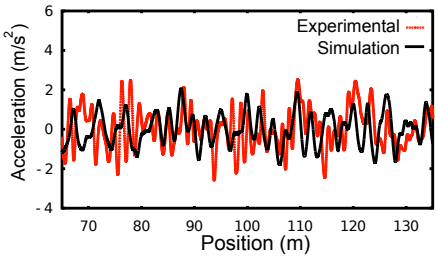

Figure 26 Floor sensor response on the East going segment. Signal filtered to preserve frequencies below 0.7 oscillation per meter of road, which corresponds to roughly 14 Hz.

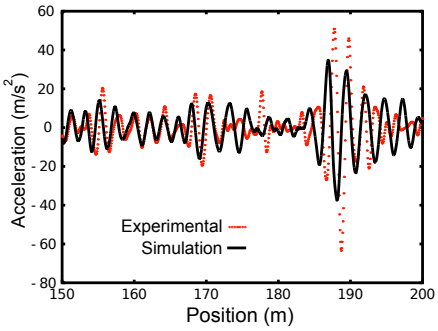

Figure 27 Rear Axle sensor response on the segment East going. Signal filtered to preserve frequencies below one oscillation per meter of road, which corresponds to roughly 20 Hz.

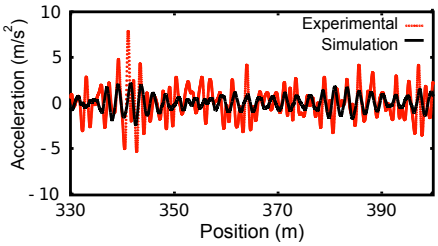

Figure 28 Lateral response of the Rear Triaxial sensor on the West going segment. Signal filtered to preserve frequencies below one oscillation per meter of road, which corresponds to roughly 20 Hz.

40 accelerometer signals; 2) calibrates itself using not only frequency responses but also position signals; and, 3) considers, calibrates, and validates energy losses. Furthermore, Wasfy *et al*. [29] show that even for simple road deformation it may be difficult to reproduce numerically the raw response of the acceleration signal.

5 Conclusion

The approach and results presented in this paper confirm that a multipurpose multibody model can assess the efficiency of a vehicle on a particular road surface. The calibration and validation of the tractor semitrailer model was done using data collected experimentally. The reproduction of the weight distribution obtained is excellent with an average error below 17 kg per wheel. The calibration of the dynamic data allowed to obtain an accurate response. The model alone reproduces correctly both the response in frequency and in position while also measuring energy losses. This is not seen elsewhere in the literature. Moreover, the quality of the responses in frequency are similar to what is expected from a multibody model even though in the present case 44 different signals are considered as opposed to the usual one or few signals. Similarly, the acceleration response versus position is adequate over the 24 km of signals calibrated. As for the energy consumption, the mean error is very small at 3% over the 4 segments studied. This is encouraging because dissipated energy is usually not considered by multibody dynamics models or when it is considered it usually

is underestimated. Also, every optimised parameter remains representative of physically sound values.

Based on the literature, the results of the validation, and further testing, the model is deemed adequate for the targeted purpose: running a virtual tractor semitrailer over a longitudinal profile with minimal steering at operating velocities between 35 km/h and 150 km/h. Given that the road profile is measured with an appropriate sampling frequency, it will allow to reproduce the truck response to punctual road deformations up to 10 cm in height and at a frequency of up to 100 Hz. These validity limits come from the tyre model. Finally, the model does yield the dynamic data which allows to measure specific vehicle impacts caused by specific longitudinal road profiles.

Acknowledgements

The authors would like to recognise the financial support of the Natural Sciences and Engineering Research Council of Canada (NSERC) and the partners of the i3C industrial research chair. The valuable involvement of Michelin®, Politecnico di Milano, Freightliner®, Manac®, the Association du camionnage du Québec and the MTQ is also recognised.

6 References

References

[1] Trucksim 8.1, 2010.

[2] C. J. Bester. The effect of road roughness on safety. In *TRB 2003 Annual Meeting*, 2003.

[3] M. Bouazara. *Étude et analyse de la suspension active et semi-active des véhicules routiers*. PhD thesis, Université Laval, 1997.

[4] Y. Delanne. The influence of pavement evenness and macrotexture on fuel consumption. In *Vehicle-road interaction*, pages 240–247. American Society for Testing and Materials, 1994.

[5] FAA. Guidelines and procedures for measuring airfield pavement roughness. AC 150/5380-9, Washington, DC, 2009.

[6] B. Falah and P.-É. Côté. Simulation et validation expérimentale de modèles du comportement dynamique de véhicules lourds. Technical report, Université du Québec à Rimouski, 2005.

[7] G. Fichera, M. Scionti, and F. Garesci. Experimental correlation between the road roughness and the comfort perceived in bus cabins. *SAE Technical Paper*, 2007.

[8] M. Fraggstedt. Power dissipation in car tyres. Technical report, Royal Institute of Technology, Stockholm, 2006.

[9] D. Gagnon, I. Beaulac, G. Doré, and P. Pierre. L'incidence de l'uni et du type de chaussée sur le coût d'opération d'un véhicule, sur l'émission des gaz à effet de serre et sur la sécurité des usagers de la route. Technical report, Transport Canada, 2006.

[10] L. Gyenes and C. G. B. Mitchell. The effect of vehicle-road interaction on fuel consumption. In *Vehicle-road interaction*, pages 225–239. American Society for Testing and Materials, 1994.

[11] D. Han. *Development of open-source hybrid pavement management system for an international standard*. PhD thesis, Kyoto University, 2011.

[12] J. G. Howe, J. P. Chrstos, R. W. Allen, T. T. Myers, D. Lee, C.-Y. Liang, and D. J. Gorsich. Quarter car model stress analysis for terrain/road profile ratings. *International Journal of Vehicle Design*, 36(2/3):248–269, 2004.

[13] N. M. Jackson. Preliminary report: An evaluation of the relationship between fuel consumption and pavement smoothness. Technical report, University of North Carolina, 2004.

[14] R. L. Jackson, J. R. Willis, M. Arnold, and C. Palmer. Synthesis of the effects of pavement properties on tire rolling resistance. Technical report, National Center for Asphalt Technology, Auburn University, Auburn, Alabama, 2011.

[15] J. McLean and G. Foley. Road surface characteristics and condition: effects on road users. Technical report, ARRB Transport Research, 1998.

[16] A. J. P. Miege and A. A. Popov. The rolling resistance of truck tyres under a dynamic vertical load. *Vehicle System Dynamics*, 43:135–144, 2005.

[17] S. Rakheja, A. K. W. Ahmed, and I. Stiharu. Urban bus optimal passive suspension study. Technical report, Concordia University, 2001.

[18] T. B. Rhyne and S. M. Cron. Tire energy loss from obstacle impact. *Tire Science and Technology*, 35(2):141–161, 2007.

[19] M. J. Richard, G. Doré, V. Vassev, and N. Fradette. Étude des conséquences de la détérioration de l'uni des chaussées sur le comportement des véhicules et la sécurité des usagers de la route. *Revue canadienne de génie civil*, 36(3):504–513, 2009.

[20] F. Romão, H. Nizamo, D. Mapasse, M. M. Rafico, J. José, S. Mataruca, M. L. Efron, L. O. Omondi, T. Leifert, and J. M. L. M. Bicho. Road traffic injuries in mozambique. *Injury Control and Safety Promotion*, 10(1-2):63–67, 2003.

[21] C. s. Xu, H. h. Yi, and C. x. Huang. Experimental study of vehicle modelling and ride comfort simulation based on the topology structure analysing. In *Proceedings of the Sixth International Conference on Intelligent Systems Design and Applications*, 2006.

[22] SAE. *Road load measurement using onboard anemometry and coastdown techniques*, volume J2263. Society of Automotive Engineers, 2008.

[23] A. Sattaripour. The effect of road roughness on vehicle behaviour. In *The dynamics of vehicles on roads and tracks*, 1977.

[24] M. W. Sayers and S. M. Karamihas. *The little book of profiling*. UMTRI, 1998.

[25] G. J. Stein, R. Zahoranský, T. P. Gunston, L. Burström, and L. Meyer. Modelling and simulation of a fore-and-aft driverâŁ™s seat suspension system with road excitation. *International Journal of Industrial Ergonomics*, 38:396–409, 2008.

[26] V. Vassev. Étude des conséquences de la détérioration de l'uni des chaussées sur le comportement des véhicules. Master's thesis, Université Laval, 2005.

[27] S. A. Velinsky and R. A. White. Vehicle energy dissipation due to road roughness. *Vehicle System Dynamics*, 9:359–384, 1980.

[28] J. C. Wambold. Road roughness effects on vehicle dynamics. In *Measuring road roughness and its effects on user cost and comfort*, pages 179–196. American Society for Testing and Materials, 1985.

[29] T. M. Wasfy, J. O'Kins, and S. Smith. Experimental validation of a coupled fluid-multibody dynamics model for tanker trucks. *SAE International Journal Commercial Vehicles*, 2008.

[30] J. P. Zaniewski and B. C. Butler. Vehicle operating costs related to operating mode, road design, and pavement condition. In *Measuring road roughness and its effects on user and comfort: a symposium*. American Society for Testing and Materials, 1985.